PCCP

ROYAL SOCIETY OF CHEMISTRY

PAPER

View Article Online
View Journal | View Issue



Cite this: *Phys. Chem. Chem. Phys.*, 2020, **22**, 9067

# HERFD-XANES probes of electronic structures of iron$^{II/III}$ carbene complexes†

Meiyuan Guo, [ab] Om Prakash, [c] Hao Fan, [c] Lisa H. M. de Groot, [c] Valtýr Freyr Hlynsson, [c] Simon Kaufhold, [c] Olga Gordivska, [c] Nicolás Velásquez, [b] Pavel Chabera, [b] Pieter Glatzel, [d] Kenneth Wärnmark, [c] Petter Persson [e] and Jens Uhlig *[b]

Iron centered *N*-heterocyclic carbene (Fe-NHC) complexes have shown long-lived excited states with charge transfer character useful for light harvesting applications. Understanding the nature of the metal–ligand bond is of fundamental importance to rationally tailor the properties of transition metal complexes. The high-energy-resolution fluorescence detected X-ray absorption near edge structure (HERFD-XANES) has been used to probe the valence orbitals of three carbene complexes, $[Fe^{II}(bpy)(btz)_2](PF_6)_2$ (bpy = 2,2′-bipyridine, btz = 3,3′-dimethyl-1,1′-bis(*p*-tolyl)-4,4′-bis(1,2,3-triazol-5-ylidene)), $[Fe^{III}(btz)_3](PF_6)_3$, and $[Fe^{III}(phtmeimb)_2]PF_6$ (phtmeimb = [phenyl(tris(3-methylimidazol-2-ylidene))borate]$^-$). The multi-configurational restrict active space (RAS) approach has been used to simulate the metal K pre-edge X-ray absorption spectroscopy of these carbene complexes, and have reproduced the metal K pre-edge spectral features in terms of relative intensity and peak positions. The evident intensity difference between the $Fe^{II}$ and the other two $Fe^{III}$ complexes has been elucidated with different intensity mechanisms in the transition. The smaller splitting between the $t_{2g}$ and $e_g$ character peak for $[Fe^{III}(btz)_3](PF_6)_3$ has been observed in the experimental measurements and been reproduced in the RAS calculations. The results show how the combination of experimental HERFD-XANES measurements and *ab initio* RAS simulations can give quantitative evaluation of the orbital interactions between metal and ligands for such large and strongly interacting systems and thus allow to understand and predict properties of novel complexes.

Received 21st November 2019,
Accepted 18th February 2020

DOI: 10.1039/c9cp06309a

rsc.li/pccp



## 1 Introduction

Transition metal complexes using ruthenium, osmium, and iridium metals are popular choices as photosensitizers or photocatalysts due to their long-lived charge transfer (CT) excited states combined with photo- and chemical stability.[1–5] However, their widespread deployment has been limited due to the rare and sometimes harmful nature of their central metal. The abundance (and low price) as well as the relatively non-toxic properties of first-row transition metals like iron make them attractive choices to replace noble metals for large-scale light-harvesting and light-emitting devices. The application of first-row transition metals has so far been hampered by the short lifetimes of CT states, which usually deactivate ultra-fast through lower-energy metal-centered (MC) states.[5–11]

Visible light excitation generates in the here discussed complexes a metal-to-ligand charge transfer (MLCT) state or a ligand-to-metal charge transfer (LMCT) state depending on the oxidation state of iron. The relative energy of the CT states and the MC states can be manipulated by *e.g.* tuning the metal–ligand interactions, for instance, by tuning the σ-donating and π-accepting strengths of the ligands.[12] Our recently developed iron complexes show long-lived (up to ns) excited states with CT character which was achieved by the use of ligands with *N*-heterocyclic carbene (NHC) moieties.[13–16] MLCT state lifetimes of 13 ps and 528 ps have been achieved for iron carbene complexes $[Fe^{II}(bpy)(btz)_2](PF_6)_2$ and $[Fe^{II}(btz)_3](PF_6)_2$ respectively,[13,15] and LMCT state lifetimes of 100 ps and 2 ns have been achieved for $[Fe^{III}(btz)_3](PF_6)_3$ and $[Fe^{III}(phtmeimb)_2]PF_6$, respectively.[14,16] These long lifetimes make iron carbene

[a] *College of Chemistry and Chemical Engineering, Southwest University, Chongqing 400715, P. R. China*
[b] *Division of Chemical Physics, Chemical Center, Lund University, SE-221 00 Lund, Sweden*
[c] *Center for Analysis and Synthesis (CAS), Department of Chemistry, Lund University, SE-22100 Lund, Sweden*
[d] *European Synchrotron Radiation Facility, 71 Avenue des Martyrs, CS 40220, 38043 Grenoble, France*
[e] *Division of Theoretical Chemistry, Chemical Center, Lund University, SE-221 00 Lund, Sweden. E-mail: jens.uhlig@chemphys.lu.se*

† Electronic supplementary information (ESI) available. See DOI: 10.1039/c9cp06309a

complexes interesting candidates as photo-sensitizers and photo-redox catalysts.[14,16]

For the design of new generations of iron carbene complexes, improved knowledge about their electronic structures is required such as how the ligands affect the valence orbitals, and how they influence the relative energies of CT and MC states involved in the excited state decay processes. X-ray absorption spectroscopy (XAS) directly probes the unoccupied and partially occupied valence orbitals through transitions from strongly localized deep core orbitals and is thus a useful method to elucidate these details.[17,18] Metal K edge XAS is usually subdivided into two regions, X-ray absorption near edge structure (XANES) and the extended X-ray fine structure (EXAFS). The transitions probed with XANES give electronic-structure information about the occupation of valence orbitals, the orbital covalency, oxidation state of metal center, and the site symmetry, which this paper is focused on. Particularly we will focus on the energetic position and intensity of the pre-edge features, as these are a direct probe of the valence orbitals. The intensity of the transition metal K pre-edge features is usually associated with dipole-forbidden electronic transitions from the 1s to the 3d orbitals. The K pre-edge intensity is obviously dependent on the number of holes in the 3d shell, another strong, sometimes even stronger influence is the character of the target molecular orbitals. Their intensity is thus a measure for the metal 3d character of the valence orbitals involved in the transitions and of the covalency of the metal–ligand bonds.[17] Apart from the metals 3d characters, the intensity can be significantly deviated by including electric-dipole transitions, back-donation charge transfers.[17,19,20] The electric quadrupole transitions are in general $\sim$2 orders of magnitude weaker than electric dipole allowed transitions, which has been shown in complexes with distorted centrosymmetry.[21] The distortion allows for the delocalization of metal 4p character into metal-3d character orbitals through orbital interaction with the ligand.

One challenge for these type of studies is that conventional metal K pre-edge spectra measured with XAS are broadened significantly due to the short lifetime of the initial 1s core hole excitation (core-hole lifetime broadening $\sim$1.25 eV for Fe).[22] This spectral broadening can often be circumvented by collecting the emitted X-ray fluorescence in a narrow energy bandwidth in a technique called high-energy-resolution fluorescence detected X-ray absorption spectroscopy (HERFD-XAS) and the measured spectrum is in many cases closely related to the XAS.[23–26]

## 2 Experimental section

The synthesis of the three carbene complexes discussed here has been described previously.[13,14,16] The powder samples were ground into a fine powder and measured undiluted in a template of homogeneous thickness between two Kapton foils. The HERFD-XAS were recorded at the ID26 beamline of the European Synchrotron Radiation Facility (ESRF) by scanning the incident beam energy with the Si(311) monochromator crystal at a fixed undulator gap, while the energy of the fluorescence detector was kept fixed at the maximum energy of Fe K$\alpha_1$ emission line. An iron foil was used to calibrate the monochromator energy to 7112 eV at the first maximum of the derivative spectrum in transmission before the first sample was measured. The absorption edge of the last sample was measured prior to this experiment and found coinciding with this measurement, excluding energy drifts within the $\sim$15 min total measurement time for all samples. The incoming flux was $\sim 10^{13}$ photons per second at a beam footprint on the sample of 0.1 (vertical) by 1 (horizontal) mm$^2$. The K$\alpha_1$ fluorescence intensity was recorded with an emission spectrometer employing the (440) reflection of four spherical ($r$ = 50 mm) Ge analyzer crystals with spherically bent 1 m radius. The width of the elastic peak giving the combined energy bandwidth was 0.65 eV. All samples were checked for damage induced by the X-rays. The statistical quality of experimental spectra are evaluated by using Poisson distributed photon statistics of the number of counts and adding an (estimated) additional 2% of the local intensity to include possible variations during the normalization. In the plots the double of this error is presented as 2$\sigma$ confidence environment.

## 3 Computational details

Calculations of molecular systems have been performed on ground state geometries (see Fig. 1) optimized using density functional theory (DFT)[27,28] with the modified hybrid functional B3LYP (15% Hartree–Fock exchange)[29] and the 6-311G(d) basis set using Gaussian 09.[30]

The calculations of X-ray absorption spectra have been performed using OpenMolcas.[31] The method for metal K pre-edge XAS has shown its validity on 3d transition metal complexes.[20,32,33] The active space used for spectra calculations could be designated as RAS($n$, $l$, $m$; $i$, $j$, $k$), where $i$, $j$, and $k$ are the number of orbitals in RAS1, RAS2, and RAS3 spaces respectively, $n$ is the total number of electrons in the active space, $l$ the maximum number of holes allowed in RAS1, and $m$ the maximum number of electrons in RAS3. For the metal K pre-edge XAS calculation, the 1s core orbital is placed in the RAS1, the five metal 3d character orbitals together with two ligand-character $\sigma$ donation orbitals and three empty orbitals of $\pi$ symmetry are placed in the RAS2, the active space is shown in Fig. 2, this gives active space RAS(12,1,0; 1,10,0) for $[Fe^{II}(bpy)(btz)_2]^{2+}$, and RAS(11,1,0; 1,9,0) for $[Fe^{III}(btz)_3]^{3+}$ and $[Fe^{III}(phtmeimb)_2]^{1+}$.

RASSCF wavefunction optimizations have been performed using the state average (SA) formalism,[34] which means that the same orbitals are used for all states of a specific spin and symmetry. Scalar relativistic effects have been included by using a second-order Douglas–Kroll–Hess Hamiltonian,[35,36] in combination with the ANO-RCC basis set and the use of a Cholesky decomposition approach to approximate the two-electron integrals.[37–39] The choice of basis set and number of final states included in which the calculations are performed is constant on all complexes. For further information on their dependency see *e.g.* Fig. S2 and S3 in the ESI.†

 

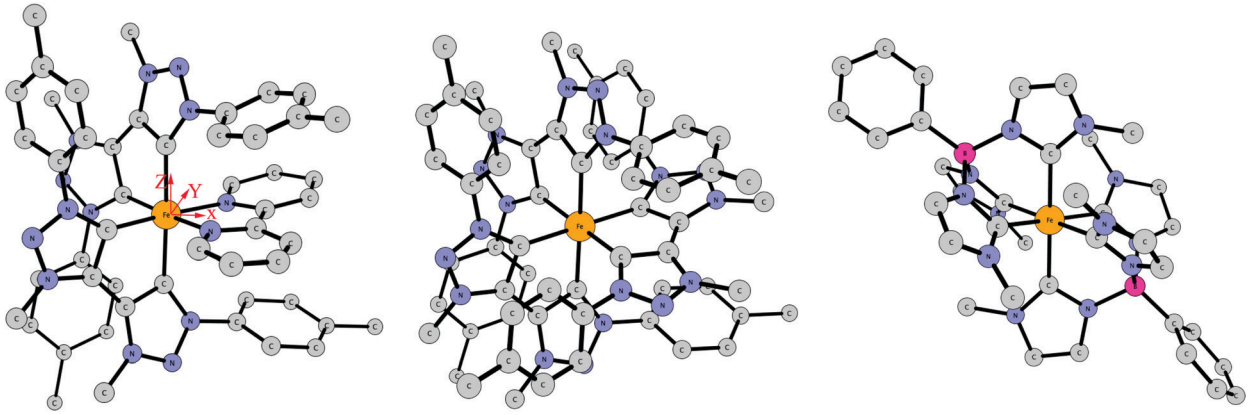

Fig. 1 The structures of carbene complexes $[Fe^{II}(bpy)(btz)_2]^{2+}$ (left), $[Fe^{III}(btz)_3]^{3+}$ (middle) and $[Fe^{III}(phtmeimb)_2]^{1+}$ (right), the iron is highlighted in yellow, boron in deep pink, nitrogen in blue and carbon in grey, the counter-ions and hydrogen atoms are not shown for clarity. The orientations of axes are indicated.

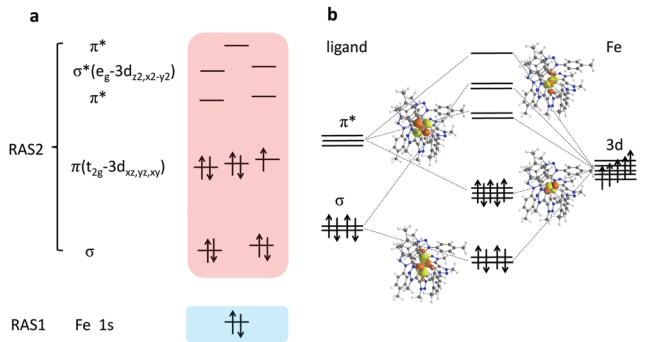


Fig. 2 (a) The RAS active space for K pre-edge XAS calculation of $Fe^{III}$ complexes, there is one more electron on orbitals for $[Fe^{II}(bpy)(btz)_2]^{2+}$. (b) Schematic orbital diagram of $[Fe^{III}(btz)_3]^{3+}$, selected valence orbitals from RAS ground state calculation are shown, the complete sets of the valence orbitals are available in Fig. S1 (ESI†).

The inclusion of dynamical correlation through second-order perturbation theory (RASPT2) calculation has been performed on $[Fe^{III}(phtmeimb)_2]^{1+}$, the spectrum is presented in Fig. S4 (ESI†). The inclusion of RASPT2 calculation only has a minor influence on the data, while significantly increasing the calculation costs.[40] Spin–orbit coupling is included by a RAS state-interaction (RASSI) approach.[41,42] Overall, the expanded basis set and the inclusion of dynamical correction have pronounced effects on the absolute incident energy, and negligible effect on the spectral shape, see Fig. S2 and S4 in the ESI.† For comparison to the experimental spectra, the simulated RAS spectra are plotted using a Lorentzian broadening with a full-width-at-half-maximum (FWHM) of 1.25 eV and further convoluted with a Gaussian broadening of 0.65 eV. The shift energy −22.15 eV is used for $[Fe^{II}(bpy)(btz)_2]^{2+}$, and −21.75 eV for both $Fe^{III}$ complexes.

## 4 Results

All three complexes have pseudo-octahedral ligand coordination and are low spin in their ground state configuration. We thus use the usual octahedral labels of $e_g$ and $t_{2g}$ for the metal 3d-like orbitals. The $[Fe^{II}(bpy)(btz)_2](PF_6)_2$ has six electrons in the three $t_{2g}$ orbitals, which gives a $t_{2g}^6e_g^0$ ground state configuration. Both $[Fe^{III}(btz)_3](PF_6)_3$ and $[Fe^{III}(phtmeimb)_2]PF_6$ have five electrons in three $t_{2g}$ orbitals and thus $t_{2g}^5e_g^0$ as ground state configuration.

The $[Fe^{II}(bpy)(btz)_2]^{2+}$ contains one bpy ligand and two btz ligands (also Fig. 1). Here the introduction of strongly σ-donating NHC ligands destabilized the lower-lying triplet and quintet MC states, while pushing away the minimum of their potential energy surface from the $^3$MLCT state, hence making an intersystem crossing in to quintet multiplicity unlikely as $^3$MLCT deactivation path as we have shown in our recent publication.[11] In $[Fe^{III}(btz)_3]^{3+}$, the bpy ligand is replaced by a third btz ligand. This replacement improves the orthoaxiality and leads to *trans* C–Fe–C angles of 179° compared to the 159° of the previously reported homoleptic NHC complexes with bis-tridentate ligand environment.[43] The improved orthoaxiality could contribute to a larger ligand field splitting, and result in a further destabilization of the MC states.[44] At the same time, the btz ligand is a stronger acceptor than bpy, which does stabilize the $t_{2g}$ orbitals further, and gives a stronger ligand field strength. The $[Fe^{III}(phtmeimb)_2]PF_6$ has a near-perfect 180° for the C–Fe–C *trans* angle. The two mono-anionic facial tris-carbene ligands have a more pronounced-donating ability and can further destabilize the $e_g$ anti-bonding molecular orbitals of metal character, and hence destabilize the quartet and sextet MC states relative to the complex $[Fe^{III}(btz)_3]^{3+}$. The MC state destabilization can contribute to the increase of activation barrier for the $^2$LMCT state decay through the MC states.

The orbital covalency analyses for the selected valence orbitals from the RASSCF ground state calculations of the three carbene complexes are presented in the Table 1. These orbital covalency analyses are performed using the Multiwfn package.[45] The characters of the selected orbitals are connected with the observed spectral features in the measurements and simulated metal K pre-edge XAS (and will be discussed in the following sections). The metal 3d and 4p characters in the targeted orbitals do reflect the electric quadrupole and dipole transition contribution intensity differences in the XAS, respectively.

Table 1 Orbital covalency (in%) for the iron carbene complexes presented in this paper. The delocalized Fe 4p components in metal 3d character molecular orbitals are shown in the parentheses

| | $\pi(3d_{xz})$ | $\pi(3d_{yz})$ | $\pi(3d_{x^2-y^2})$ | $\sigma(3d_{xy})$ | $\sigma(3d_{z^2})$ |
|---|---|---|---|---|---|
| $[Fe^{II}(bpy)(btz)_2]^{2+}$ | 86.3 | 82.6 | 82.0 | 62.4(0.52) | 62.3(1.4) |
| $[Fe^{III}(btz)_3]^{3+}$ | 86.5 | 94.3 | 86.5 | 56.3(<0.5) | 56.2(<0.5) |
| $[Fe^{III}(phtmeimb)_2]^{1+}$ | 67.0 | 94.3 | 85.6 | 56.8(<0.5) | 56.9(<0.5) |

### 4.1 Observations in the experimental HERFD-XANES

The $[Fe^{II}(bpy)(btz)_2](PF_6)_2$ has a $t_{2g}^6e_g^0$ ground state configuration with fully filled $t_{2g}$ orbitals. The experimental K pre-edge of $[Fe^{II}(bpy)(btz)_2](PF_6)_2$ thus shows one dominant peak at 7113.6 eV which originates from the 1s to $e_g$ transitions, see Fig. 3. The very small feature at 7111.6 eV, a fingerprint for the $1s \rightarrow t_{2g}$ of the $Fe^{III}$ oxidation state is likely due to impurities in the sample. For the full measured spectra see the Fig. S5 (ESI†).

Both $Fe^{III}$ complexes show the classical strong two-peaks features originating from the 1s core electron transition to $t_{2g}$ and $e_g$, respectively. The $t_{2g}$ peak of $[Fe^{III}(phtmeimb)_2]PF_6$ shifts by ~0.2 eV compared to the $t_{2g}$ peak of $[Fe^{III}(btz)_3](PF_6)_3$, see Fig. 3. Both $Fe^{III}$ complexes also have clearly separated and broad $e_g$ features which originate from the multiplet structures of the valence shell. The energy difference between the different $e_g$ peaks is a measure of the difference of the attraction between the hole in a $t_{2g}$ orbital and the electron in a $e_g$ orbital but is also influenced by the orbital covalency.[20] This fine splitting is usually not resolved in the conventional metal K pre-edge XAS due to the large lifetime broadening. The $e_g$ peak of $[Fe^{II}(bpy)(btz)_2](PF_6)_2$ is located at lower energy compared to the $e_g$ peak of the $Fe^{III}$ complexes. Recently this energy shift has been explained by the difference in contraction of the 3d shell in the core-excited states.[46]

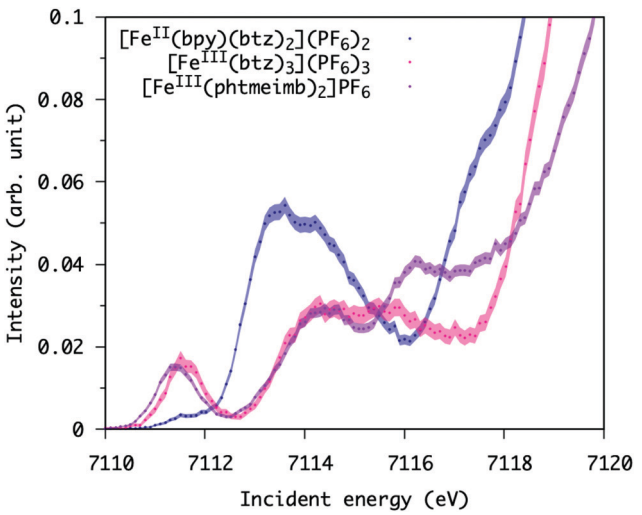


Fig. 3 The experimental iron HERFD-XANES K pre-edge features of $[Fe^{II}(bpy)(btz)_2](PF_6)_2$, $[Fe^{III}(btz)_3](PF_6)_3$ and $[Fe^{III}(phtmeimb)_2]PF_6$. The transparent filled curves represent the $2\sigma$ confidence environment of the measurement including statistical error and normalisation error. The full HERFD-XAS spectra of those complexes are available in Fig. S5 (ESI†).

### 4.2 Intensity contribution analysis

The distortion from centrosymmetry delocalizes some metal 4p orbital components into metal 3d orbitals through their interactions with the ligand orbitals. The heteroleptic $[Fe^{II}(bpy)(btz)_2](PF_6)_2$ complex has two btz ligands and one bpy ligand, which creates a less centrosymmetric environment around the iron center compared to the other two homoleptic $Fe^{III}$ complexes that are coordinated with tris-bidentate or bis-tridentate all-NHC ligands. The $[Fe^{II}(bpy)(btz)_2](PF_6)_2$ complex has $C_2$ symmetry in the calculation, the 4p orbitals can mix with $d_{xy}$ and $d_{z^2}$ orbitals under $C_2$ symmetry. The near-perfect octahedral symmetry for the $Fe^{III}$ complexes is purposefully designed to achieve large octahedral ligand field splitting.[14,16] The intensity of transitions with $e_g$ character peak for the $[Fe^{II}(bpy)(btz)_2](PF_6)_2$ at almost double intensity compared to the respective peaks in the other two $Fe^{III}$ complexes. The analysis of the orbital character of the valence orbitals in the ground state complexes showed that the molecular orbitals with $e_g$ character of $[Fe^{II}(bpy)(btz)_2]^{2+}$ have ~2% Fe 4p character. The larger number of iron 4p components in $[Fe^{II}(bpy)(btz)_2]^{2+}$ are expected as it has less orthoaxiality, which allows the iron 4p to delocalize into the 3d-like orbitals. This has an substantial effect on the intensity of this feature due to the now allowed $1s \rightarrow e_g$ (4p) electric dipole transitions. These features were well reproduced by the RAS calculations of the three iron carbene complexes (Fig. 4), which show a clear intensity difference in the peak originating from transitions into orbitals with $e_g$ character between $[Fe^{II}(bpy)(btz)_2]^{2+}$ and the $Fe^{III}$ complexes as can be seen in Fig. 4 and 5.

The 3d–4p orbital hybridization effect on the K pre-edge XAS has been well described through the RAS calculations. The integrated intensity for the calculated electric dipole contribution is $2.72 \times 10^{-4}$, $2.76 \times 10^{-6}$ and $2.79 \times 10^{-5}$ for $[Fe^{II}(bpy)(btz)_2]^{2+}$, $[Fe^{III}(btz)_3]^{3+}$ and $[Fe^{III}(phtmeimb)_2]^{1+}$, respectively. The large difference in the electric dipole transition intensity does explain the intensity difference for the measured metal K pre-edge between the $Fe^{II}$ and $Fe^{III}$ complexes in Fig. 5.

Considering that ~2% 4p characters give $2.72 \times 10^{-4}$ intensity for $[Fe^{II}(bpy)(btz)_2]^{2+}$, the 4p character of both $Fe^{III}$ complexes should be less than 0.2%, as was indeed found. At this level small variations originating from *e.g.* differences between the computationally optimized and the experimentally present structure, contributions of the solvent or of the limited basis set can have an unrealistically large effect. One would *e.g.* expect that the near perfect orthoaxiality of $[Fe^{III}(phtmeimb)_2]^{1+}$ results in the smallest dipole contribution. Conversely, if the contribution of 4p character is larger than 0.5% this is significant and differences at this level can be used to draw conclusion about symmetry effects. Future extensions and experience with this novel approach will increase the precision.

Here the relative contribution from electric dipole transitions beyond this limitation can hence be used to estimate the distortion from the centrosymmetry in the K edge measurements of octahedral complexes.

### 4.3 Discussion

The K pre-edge intensities depend on the metal 3d character in the probed valence orbitals, and can thus be used to evaluate

 

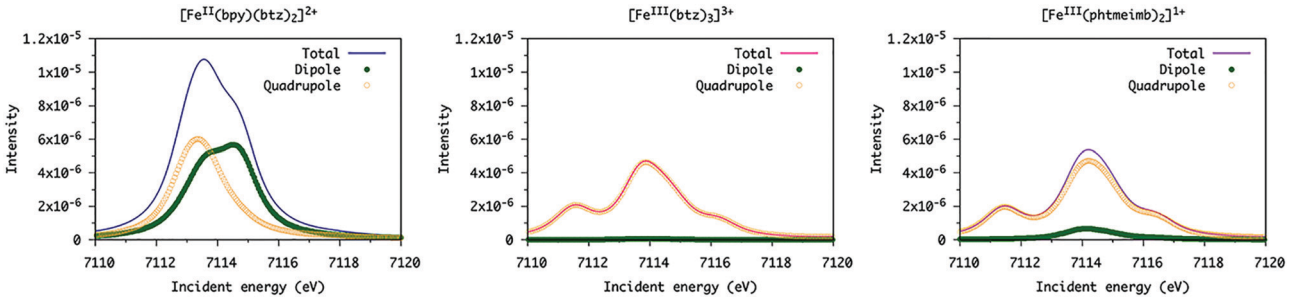


Fig. 4 The RAS calculated metal K pre-edge XAS of $[Fe^{II}(bpy)(btz)_2]^{2+}$ (left), $[Fe^{III}(btz)_3]^{3+}$ (middle) and $[Fe^{III}(phtmeimb)_2]^{1+}$ (right). The electric dipole (green) and quadrupole (yellow) contributions have been presented with dotted curves.

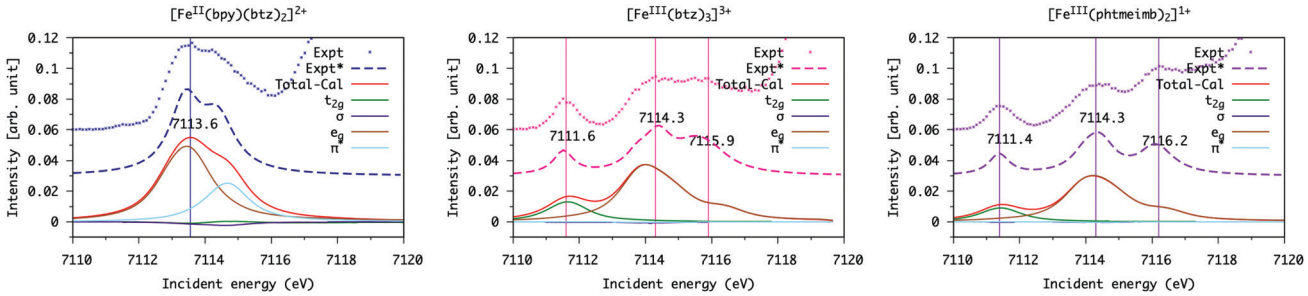


Fig. 5 The orbital contribution analysis to the RAS calculated metal K pre-edge XAS of carbene complexes $[Fe^{II}(bpy)(btz)_2]^{2+}$ (left), $[Fe^{III}(btz)_3]^{3+}$ (middle) and $[Fe^{III}(phtmeimb)_2]^{1+}$ (right). The Expt* is the background subtracted experimental spectrum using EXAFSPAK,[48] the components for fitting the metal K pre-edge are available in Fig. S6 (ESI†).

the orbital covalency and centrosymmetry of the complexes. The metal K pre-edge analyses in terms of the chemically intuitive molecular orbitals and their occupation numbers are the starting point for the comparison. The differences in occupation numbers between the ground state and each final state allows for an interpretation of the spectrum in terms of orbital excitations.[20,47] For the iron carbene molecules discussed here the contributions of individual orbitals are shown in Fig. 5.

The first absorption peak for both $Fe^{III}$ complexes originates from the 1s $\rightarrow$ $t_{2g}$ transition, their integrated intensities from calculated spectra are $0.58 \times 10^{-4}$ and $0.48 \times 10^{-4}$ for $[Fe^{III}(btz)_3]^{3+}$ and $[Fe^{III}(phtmeimb)_2]^{1+}$, which is consistent with the amount of $t_{2g}$ character of the states (see Table 1). This orbital covalency analysis shows that the metal $e_g$ character of the molecular orbital for the three complexes follows the order $[Fe^{II}(bpy)(btz)_2]^{2+} > [Fe^{III}(phtmeimb)_2]^{1+} > [Fe^{III}(btz)_3]^{3+}$ (see Table 1). The integrated intensities of electronic quadrupole transitions for the 1s $\rightarrow$ $e_g$ are $2.41 \times 10^{-4}$, $2.25 \times 10^{-4}$, and $2.15 \times 10^{-4}$ for $[Fe^{II}(bpy)(btz)_2]^{2+}$, $[Fe^{III}(phtmeimb)_2]^{1+}$ and $[Fe^{III}(btz)_3]^{3+}$, respectively. The consistent trend in intensity and the metal 3d characters in the probed orbitals shows that the molecular orbital based RAS approach can well interpret the XAS in terms of the orbital covalency.

For $Fe^{III}$, the peak with $e_g$ character is significantly broader due to the extra hole in the $t_{2g}$ orbital. After electron excitation into the empty $e_g$ orbital, the orbital occupancy of $t_{2g}^5e_g^1$ can give $^3T_{1g}$, $^3T_{2g}$, $^1T_{1g}$, and $^1T_{2g}$ valence states due to the coupling of the holes in both $t_{2g}$ and $e_g$ orbitals. The $^3T_{1g}$ and $^3T_{2g}$ triplets imply two electrons with parallel spin in the valence shell, the RAS calculations allow for multiple excitation within the active space and hence can give a nice description of the electron–electron interactions in the valence shell. Thus the broad feature splits into two main resonances at 7114.3 eV and 7115.9 eV for $[Fe^{III}(btz)_3]^{3+}$, at 7114.3 eV and 7116.2 eV for $[Fe^{III}(phtmeimb)_2]^{1+}$.

The calculated spectra gave a splitting energy of 2.0 eV for $[Fe^{III}(btz)_3]^{3+}$, and 2.1 eV for $[Fe^{III}(phtmeimb)_2]^{1+}$, which is slightly larger than was experimentally observed. RAS calculations need an increasing number of core-excited states to fully describe the spectral features at the high energy side. Beyond a certain limit, an increasing of the number of included states only slightly shifts the observed averaged spectral features, which is taken as the cut-off point for the calculations (see ESI† for an estimation of this effect). An increase of this cutoff as well as an increase of the basis set can thus theoretically result in small additional shifts of the spectrum at the price of a significantly increased computational cost. For such large molecules as are studied here, the here employed combination of number of states and basis set is currently at the limit of our computational capabilities.

The difference in splitting between the $T_{1g}$ and $T_{2g}$ states probe the difference in attraction between the hole in the $\pi(t_{2g})$ orbital and the electron in the $\sigma(3d_{xy})$ compared to the $\sigma(3d_{z^2})$. The resonance at higher energy 7115.9 eV and 7116.2 eV is assigned to the $^1T_{2g}$ state, and it shows that the splitting of these two resonances depends on the orbital covalency.[17,19,20] Considering the lower energy $t_{2g}$ peak for $[Fe^{III}(phtmeimb)_2]^{1+}$, we can conclude that the splitting between the $t_{2g}$ peak and $e_g$ peak is larger for $[Fe^{III}(phtmeimb)_2]^{1+}$. This was expected since

the adoption of $[phtmeimb]^{1-}$ ligand for a more pronounced σ donating ability can further increase the relative energy of $e_g$ metal 3d character anti-bonding orbitals, which gives a larger ligand field splitting.[16] Previous calculations have shown that the minimum energies of $^4$MC and $^6$MC states of $[Fe^{III}(phtmeimb)_2]^{1+}$ are destabilized by 13% and 23% compared to the ones of $[Fe^{III}(btz)_3]^{3+}$.[16] The $^2$LMCT state of $[Fe^{III}(phtmeimb)_2]^{1+}$ (2.13 eV) is 0.17 eV lower than the $[Fe^{III}(btz)_3]^{3+}$ (2.30 eV). The increased energies of the MC states together with the decreased energy of the $^2$LMCT state gives an increased activation barrier for the decay of the $^2$LMCT state into the MC states, and consequently contributes to the increase in the experimentally observed lifetime of the $^2$LMCT state.[14,16] The RAS calculated spectra have well reproduced the larger splitting between the $t_{2g}$ and the first resonance of the $e_g$ peak for $[Fe^{III}(phtmeimb)_2]^{1+}$, see Fig. 5, and show that this method can be used to predict the influence of new ligand systems on the energetic landscape of novel molecules. This means that we can both measure the relative energies of the valence orbitals with HERFD-XANES or calculate them prior to the synthesis with RAS and can expect to achieve an at least qualitatively good agreement even if the centrosymmetry is significantly changed. With further improvements in calculation power and code optimization this tool can potentially be extended to be used on real photocatalytical systems.

## 5 Conclusions

The ground state characterization of three iron complexes, of $[Fe^{II}(bpy)(btz)_2]^{2+}$, $[Fe^{III}(btz)_3]^{3+}$ and $[Fe^{III}(phtmeimb)_2]^{1+}$ have been carried out through the combination of experimental measurements of HERFD-XANES and were combined with *ab initio* RAS simulations of the K pre-edge XAS. We observed a large intensity difference in the $Fe^{II}$ and $Fe^{III}$ experimental HERFD-XANES and interpreted them by differences of the electric dipole contributions originating in a change of state mixing, covalency changes and symmetry changes. The multiplet effect features in the HERFD-XANES of $Fe^{III}$ complexes were resolved and nicely described through the RAS calculations. We have shown that the estimation of the electric dipole contribution and quadrupole contributions can be used to probe the distortion from centrosymmetry of these hexacoordinated complexes. The slightly low-lying $t_{2g}$ and the relatively destabilized $e_g$ orbitals of $[Fe^{III}(phtmeimb)_2]^{1+}$ were reproduced and their originating chemical differences identified. This nicely shows that RAS can be used as an predictive as well as an analytic tool even in these large complexes and can be verified with HERFD-XANES. We expect that by using this tool we can predict the effect of new ligand systems on the complex electronic environment of next generation of iron carbene complexes.

## Conflicts of interest

There are no conflicts to declare.

## Acknowledgements

We acknowledge financial support from the Knut and Alice Wallenberg foundation, the Carl Tryggers Stiftelse för Vetenskaplig Forskning and Crafoordska Stiftelsen. P. P. and K. W. acknowledge support from the Swedish Research Council (VR), the Swedish Energy Agency (Energimyndigheten), and the Swedish Foundation for Strategic Research (SSF). S. K gratefully acknowledges a scholarship from Wenner-Gren Stiftelserna (The Wenner-Gren Foundations). The computations were performed on resources provided by National Supercomputer Centre at Linköping University (Tetralith) under projects snic2018-7-47 and snic2018-3-498, and snic2018-6-42 at Lund University (Lunarc). The experiments were performed on beamline ID26 at the European Synchrotron Radiation Facility (ESRF), Grenoble, France. We are grateful to P. G. at the ESRF for providing assistance with this project.

## References

1 I. M. Dixon, J.-P. Collin, J.-P. Sauvage, L. Flamigni, S. Encinas and F. Barigelletti, *Chem. Soc. Rev.*, 2000, **29**, 385–391.
2 D. W. Thompson, A. Ito and T. J. Meyer, *Pure Appl. Chem.*, 2013, **85**, 1257–1305.
3 A. Bolje, S. Hohloch, M. van der Meer, J. Košmrlj and B. Sarkar, *Chem. – Eur. J.*, 2015, **21**, 6756–6764.
4 A. Bolje, S. Hohloch, J. Košmrlj and B. Sarkar, *Dalton Trans.*, 2016, **45**, 15983–15993.
5 C. S. Ponseca, P. Chábera, J. Uhlig, P. Persson and V. Sundström, *Chem. Rev.*, 2017, **117**, 10940–11024.
6 A. Hauser, *Spin crossover in transition metal compounds II*, Springer, 2004, pp. 155–198.
7 J. E. Monat and J. K. McCusker, *J. Am. Chem. Soc.*, 2000, **122**, 4092–4097.
8 W. Gawelda, A. Cannizzo, V.-T. Pham, F. van Mourik, C. Bressler and M. Chergui, *J. Am. Chem. Soc.*, 2007, **129**, 8199–8206.
9 C. Consani, M. Prémont-Schwarz, A. ElNahhas, C. Bressler, F. van Mourik, A. Cannizzo and M. Chergui, *Angew. Chem., Int. Ed.*, 2009, **48**, 7184–7187.
10 W. Zhang and K. J. Gaffney, *Acc. Chem. Res.*, 2015, **48**, 1140–1148.
11 H. Tatsuno, K. S. Kjær, K. Kunnus, T. C. B. Harlang, C. Timm, M. Guo, P. Chábera, L. A. Fredin, R. W. Hartsock and M. E. Reinhard, *et al.*, *Angew. Chem., Int. Ed.*, 2019, 372–380.
12 Y. Liu, P. Persson, V. Sundström and K. Wärnmark, *Acc. Chem. Res.*, 2016, **49**, 1477–1485.
13 Y. Liu, K. S. Kjær, L. A. Fredin, P. Chabera, T. Harlang, S. E. Canton, S. Lidin, J. Zhang, R. Lomoth and K.-E. Bergquist, *Chem. – Eur. J.*, 2015, **21**, 3628–3639.
14 P. Chábera, Y. Liu, O. Prakash, E. Thyrhaug, A. El Nahhas, A. Honarfar, S. Essen, L. A. Fredin, T. C. Harlang and K. S. Kjær, *et al.*, *Nature*, 2017, **543**, 695.
15 P. Chábera, K. S. Kjær, O. Prakash, A. Honarfar, Y. Liu, L. A. Fredin, T. C. Harlang, S. Lidin, J. Uhlig and V. Sundström, *J. Phys. Chem. Lett.*, 2018, **9**, 459–463.
16 K. S. Kjær, N. Kaul, O. Prakash, P. Chábera, N. W. Rosemann, A. Honarfar, O. Gordivska, L. A. Fredin, K.-E. Bergquist and L. Häggström, *et al.*, *Science*, 2019, **363**, 249–253.

17 T. E. Westre, P. Kennepohl, J. G. DeWitt, B. Hedman, K. O. Hodgson and E. I. Solomon, *J. Am. Chem. Soc.*, 1997, **119**, 6297–6314.
18 F. Ericson, A. Honarfar, O. Prakash, H. Tatsuno, L. A. Fredin, K. Handrup, P. Chabera, O. Gordivska, K. S. Kjær, Y. Liu, J. Schnadt, K. Wärnmark, V. Sundström, P. Persson and J. Uhlig, *Chem. Phys. Lett.*, 2017, **683**, 559–566.
19 M. Lundberg, T. Kroll, S. DeBeer, U. Bergmann, S. A. Wilson, P. Glatzel, D. Nordlund, B. Hedman, K. O. Hodgson and E. I. Solomon, *J. Am. Chem. Soc.*, 2013, **135**, 17121–17134.
20 M. Guo, L. K. Sørensen, M. G. Delcey, R. V. Pinjari and M. Lundberg, *Phys. Chem. Chem. Phys.*, 2016, **18**, 3250–3259.
21 T. Yamamoto, *X-Ray Spectrom.*, 2008, **37**, 572–584.
22 M. O. Krause and J. Oliver, *J. Phys. Chem. Ref. Data*, 1979, **8**, 329–338.
23 P. Glatzel, T.-C. Weng, K. Kvashnina, J. Swarbrick, M. Sikora, E. Gallo, N. Smolentsev and R. A. Mori, *J. Electron Spectrosc. Relat. Phenom.*, 2013, **188**, 17–25.
24 K. Hämäläinen, D. Siddons, J. Hastings and L. Berman, *Phys. Rev. Lett.*, 1991, **67**, 2850.
25 P. Glatzel and U. Bergmann, *Coord. Chem. Rev.*, 2005, **249**, 65–95.
26 M. Bauer, *Phys. Chem. Chem. Phys.*, 2014, **16**, 13827–13837.
27 P. Hohenberg and W. Kohn, *Phys. Rev.*, 1964, **136**, B864.
28 W. Kohn and L. J. Sham, *Phys. Rev.*, 1965, **140**, A1133.
29 A. D. Becke, *Phys. Rev. A: At., Mol., Opt. Phys.*, 1988, **38**, 3098.
30 M. J. Frisch, G. W. Trucks, H. B. Schlegel, G. E. Scuseria, M. A. Robb, J. R. Cheeseman, G. Scalmani, V. Barone, B. Mennucci, G. A. Petersson, H. Nakatsuji, M. Caricato, X. Li, H. P. Hratchian, A. F. Izmaylov, J. Bloino, G. Zheng, J. L. Sonnenberg, M. Hada, M. Ehara, K. Toyota, R. Fukuda, J. Hasegawa, M. Ishida, T. Nakajima, Y. Honda, O. Kitao, H. Nakai, T. Vreven, J. A. Montgomery, Jr., J. E. Peralta, F. Ogliaro, M. Bearpark, J. J. Heyd, E. Brothers, K. N. Kudin, V. N. Staroverov, R. Kobayashi, J. Normand, K. Raghavachari, A. Rendell, J. C. Burant, S. S. Iyengar, J. Tomasi, M. Cossi, N. Rega, J. M. Millam, M. Klene, J. E. Knox, J. B. Cross, V. Bakken, C. Adamo, J. Jaramillo, R. Gomperts, R. E. Stratmann, O. Yazyev, A. J. Austin, R. Cammi, C. Pomelli, J. W. Ochterski, R. L. Martin, K. Morokuma, V. G. Zakrzewski, G. A. Voth, P. Salvador, J. J. Dannenberg, S. Dapprich, A. D. Daniels, O. Farkas, J. B. Foresman, J. V. Ortiz, J. Cioslowski and D. J. Fox, *Gaussian09 Revision E.01*, Gaussian Inc., Wallingford CT, 2009.
31 I. Fdez. Galván, M. Vacher, A. Alavi, C. Angeli, F. Aquilante, J. Autschbach, J. J. Bao, S. I. Bokarev, N. A. Bogdanov, R. K. Carlson, L. F. Chibotaru, J. Creutzberg, N. Dattani, M. G. Delcey, S. S. Dong, A. Dreuw, L. Freitag, L. M. Frutos, L. Gagliardi, F. Gendron, A. Giussani, L. González, G. Grell, M. Guo, C. E. Hoyer, M. Johansson, S. Keller, S. Knecht, G. Kovačević, E. Källman, G. Li Manni, M. Lundberg, Y. Ma, S. Mai, J. A. P. Malhado, P. A. Malmqvist, P. Marquetand, S. A. Mewes, J. Norell, M. Olivucci, M. Oppel, Q. M. Phung, K. Pierloot, F. Plasser, M. Reiher, A. M. Sand, I. Schapiro, P. Sharma, C. J. Stein, L. K. Sørensen, D. G. Truhlar, M. Ugandi, L. Ungur, A. Valentini, S. Vancoillie, V. Veryazov, O. Weser, T. A. Wesołowski, P.-O. Widmark, S. Wouters, A. Zech, J. P. Zobel and R. Lindh, *J. Chem. Theory Comput.*, 2019, **15**, 5925–5964.
32 L. K. Sørensen, M. Guo, R. Lindh and M. Lundberg, *Mol. Phys.*, 2017, **115**, 174–189.
33 M. Guo, E. Källman, L. K. Sørensen, M. G. Delcey, R. V. Pinjari and M. Lundberg, *J. Phys. Chem. A*, 2016, **120**, 5848–5855.
34 P. Å. Malmqvist, A. Rendell and B. O. Roos, *J. Phys. Chem.*, 1990, **94**, 5477–5482.
35 M. Douglas and N. M. Kroll, *Ann. Phys.*, 1974, **82**, 89–155.
36 B. A. Hess, *Phys. Rev. A: At., Mol., Opt. Phys.*, 1986, **33**, 3742.
37 B. O. Roos, R. Lindh, P.-Å. Malmqvist, V. Veryazov and P.-O. Widmark, *J. Phys. Chem. A*, 2004, **108**, 2851–2858.
38 B. O. Roos, R. Lindh, P.-Å. Malmqvist, V. Veryazov and P.-O. Widmark, *J. Phys. Chem. A*, 2005, **109**, 6575–6579.
39 J. Boström, M. G. Delcey, F. Aquilante, L. Serrano-Andrés, T. B. Pedersen and R. Lindh, *J. Chem. Theory Comput.*, 2010, **6**, 747–754.
40 R. V. Pinjari, M. G. Delcey, M. Guo, M. Odelius and M. Lundberg, *J. Comput. Chem.*, 2016, **37**, 477–486.
41 P.-Å. Malmqvist and B. O. Roos, *Chem. Phys. Lett.*, 1989, **155**, 189–194.
42 P.-Å. Malmqvist, B. O. Roos and B. Schimmelpfennig, *Chem. Phys. Lett.*, 2002, **357**, 230–240.
43 Y. Liu, T. Harlang, S. E. Canton, P. Chábera, K. Suárez-Alcántara, A. Fleckhaus, D. A. Vithanage, E. Göransson, A. Corani and R. Lomoth, *Chem. Commun.*, 2013, **49**, 6412–6414.
44 S. Campagna, F. Puntoriero, F. Nastasi, G. Bergamini and V. Balzani, *Photochemistry and Photophysics of Coordination Compounds I*, Springer, 2007, pp. 117–214.
45 T. Lu and F. Chen, *J. Comput. Chem.*, 2012, **33**, 580–592.
46 M. Kubin, M. Guo, T. Kroll, H. Löchel, E. Källman, M. L. Baker, R. Mitzner, S. Gul, J. Kern and A. Föhlisch, *Chem. Sci.*, 2018, **9**, 6813–6829.
47 R. V. Pinjari, M. G. Delcey, M. Guo, M. Odelius and M. Lundberg, *J. Chem. Phys.*, 2014, **141**, 124116.
48 G. N. George and I. J. Pickering, *EXAFSPAK: A suite of computer programs for analysis of X-ray absorption spectra*, SSRL, Stanford, 1995.